Nuclear Science and Techniques (2024) 35:200
https://doi.org/10.1007/s41365-024-01576-1

Check for updates

Fudan multi-purpose active target time projection chamber (fMeta-TPC) for photonuclear reaction experiments

Huang-Kai Wu[1] · Xi-Yang Wang[1] · Yu-Miao Wang[1] · You-Jing Wang[1] · De-Qing Fang[1] · Wan-Bing He[1] · Wei-Hu Ma[1] · Xi-Guang Cao[2,3,4] · Chang-Bo Fu[1] · Xian-Gai Deng[1,5] · Yu-Gang Ma[1,5]

Received: 18 June 2024 / Revised: 17 July 2024 / Accepted: 28 July 2024 / Published online: 13 October 2024

Abstract

Active target time projection chambers are state-of-the-art tools in the field of low-energy nuclear physics and are particularly suitable for experiments using low-intensity radioactive ion beams or gamma rays. The Fudan multi-purpose active target time projection chamber (fMeta-TPC) with 2048 channels was developed to study α-clustering nuclei. This study focused on the photonuclear reaction with a laser Compton scattering gamma source, particularly for the decay of the highly excited α cluster state. The design of fMeta-TPC is described in this paper. A comprehensive evaluation of its offline performance was conducted using an ultraviolet laser and ^{241}Am α source. The results showed that the intrinsic angular resolution of the detector was within 0.30°, and the detector had an energy resolution of 6.85% for 3.0 MeV α particles. The gain uniformity of the detector was approximately 10% (RMS/Mean), as tested by the ^{55}Fe X-ray source.

Keywords Active target · Time projection chambers · Photonuclear reaction · α cluster

1 Introduction

Recently, the establishment of the Shanghai laser electron gamma source (SLEGS) beamline at the Shanghai Synchrotron Radiation Facility has provided a promising platform for studying MeV-level photonuclear reactions in China [1]. The laser Compton scattering gamma source offers advantages over traditional γ-ray sources, including quasi-monoenergetic, high brightness, and high polarization. Photonuclear reactions, which are characterized by simple reaction mechanisms and clean final-state products, serve as effective probes for nuclear structures and aid in the measurement of key reaction rates in nuclear astrophysics [2–8]. However, the most important photonuclear reaction experiments suffer from the drawbacks of small reaction cross sections and low-energy reaction products.

Active target time projection chambers (AT-TPCs) play a crucial role in low-energy nuclear physics and are considered novel and powerful detector tools [9–11]. They have been widely used in various fields, such as the ACTAR TPC of the Grand Accélérateur National d'Ions Lourds for studying shell evolution [12]; O-TPC of the University of Warsaw for studying cluster structure [13], nuclear astrophysics [14], and exotic decay [15]; MAIKo

This work is supported by the National Key R&D Program of China (Nos. 2022YFA1602402, 2020YFE0202001, and 2023YFA1606900), and the National Natural Science Foundation of China (NSFC) (Nos. 12235003, 11835002, 11925502, 11705031, 12275053, and 12147101).

✉ Chang-Bo Fu
cbfu@fudan.edu.cn

Xian-Gai Deng
xiangai_deng@fudan.edu.cn

Yu-Gang Ma
mayugang@fudan.edu.cn

1 Key Laboratory of Nuclear Physics and Ion-Beam Application (MOE), Institute of Modern Physics, Fudan University, Shanghai 200433, China

2 Shanghai Institute of Applied Physics, Chinese Academy of Sciences, Shanghai 201800, China

3 University of Chinese Academy of Sciences, Beijing 100049, China

4 Shanghai Advanced Research Institute, Chinese Academy of Sciences, Shanghai 201210, China

5 Shanghai Research Center for Theoretical Nuclear Physics, NSFC and Fudan University, Shanghai 200438, China

of Kyoto University for studying shell evolution and cluster structure [16, 17]; CAT-TPC of Peking University for studying cluster structures in unstable nuclei [18]; MATE of the Institute of Modern Physics, Chinese Academy of Sciences for studying heavy-ion fusion reactions at stellar energies [19, 20]; MTPC of the Institute of High Energy Physics, Chinese Academy of Sciences for measuring cross sections of neutron-induced light-charged particle emission and fission reactions [21, 22]; and TexAT of Texas A&M University for studying shell evolution and nuclear astrophysics [23]. AT-TPCs are designed to simultaneously use different gases as targets and detectors, providing nearly 4π solid angle coverage and a low-energy detection threshold. Furthermore, because the target itself serves as the detector, a thicker target does not compromise the energy resolution and detection efficiency, which is particularly beneficial for photonuclear reactions and low-intensity beam experiments.

AT-TPCs are particularly useful for nuclear cluster studies. The study of cluster structures in light nuclei represents a prominent research frontier in nuclear physics [24–31]. A well-known example is the Hoyle state of ^{12}C, which was first posited by F. Hoyle in 1953 to explain nucleosynthesis in stars [32]. Although various studies have indicated the presence of significant cluster components in the ground and low-lying excited states of light α-conjugate nuclei [13, 33, 34], the exact properties and configurations of α clusters remain elusive. Questions remain regarding the distinction between α cluster states and free α particles and whether α clusters adopt a Bose-Einstein condensate state [35–37] or specific geometric configurations [38–40]. Thus, the properties and structures of clusters in α-conjugated nuclei, such as ^{12}C, ^{16}O, and ^{20}Ne, and non-α-conjugated nuclei, such as ^{6}Li and ^{9}Be, including the Hoyle state in ^{12}C and analogous Hoyle-like cluster states in other α-conjugated nuclei [37, 41, 42], is an important open question.

Considering these advantages, an AT-TPC, namely, the Fudan multi-purpose active target time projection chamber (fMeta-TPC), was built. The fMeta-TPC was designed and constructed with a special focus on the study of photonuclear reactions, particularly the properties of α clusters in the excited states of light nuclei.

The remainder of this article is organized as follows: In Sect. 2 we describe the design of the fMeta-TPC. The features of the readout board are presented in Sect. 2.2, and the design and simulation of the electronic field uniformity of the field cage are presented in Sect. 2.3. An overview of the electronic system and its basic performance characteristics is provided in Sect. 2.4. Offline performance tests of the detector covering the electron drift velocity, electronic field homogeneity, angular resolution, and energy resolution of the TPC are detailed in Sect. 3. Finally, a summary is provided in Sect. 4.

2 Design of fMeta-TPC

The fMeta-TPC was developed at Fudan University, Shanghai, China. The four main components of the fMeta-TPC are the gas chamber, anode pad plane, field cage, and electronic system. A schematic view is shown in Fig. 1.

2.1 Gas chamber

As shown in Fig. 1, fMeta-TPC is housed in a cubic stainless steel chamber with a volume of 600 mm $(L) \times 450$ mm $(W) \times 475$ mm (H). This chamber is equipped with five removable flanges, located at the bottom and along the four sides, to allow easy mounting and testing of the detectors. On the beam injection side, the flange has a circular entrance window, with a diameter of 15 mm, and four quartz windows. A 0.3 mm thick Kapton foil capable

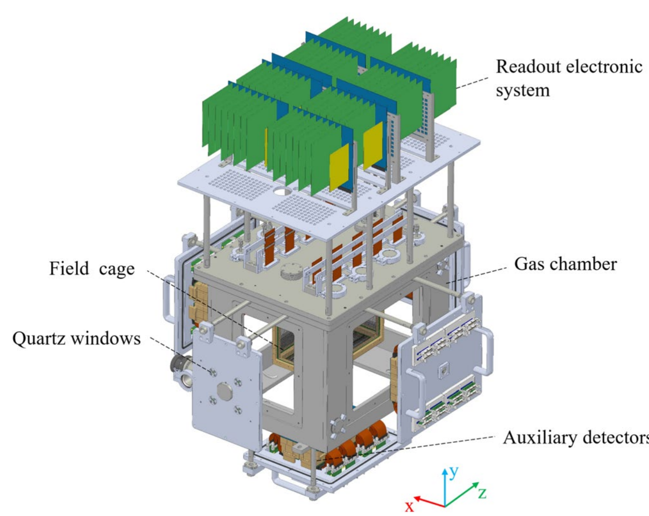

Fig. 1 3D schematic view of fMeta-TPC. (Color figure online)

of withstanding a pressure differential of 1 atm is used to maintain isolation between the gas volume and the external environment. Owing to the low stopping power of the gas, charged particles with several MeV energy can easily escape from the field cage. In view of future experimental plans regarding rare isotope beams, the remaining flanges were designed to support auxiliary detectors. For example, ΔE-E telescopes composed of a double sided silicon strip detector and a 50 mm thick CsI(Tl) detector were designed; however, these have not been described in this paper.

2.2 Resistive micromegas

As shown in Fig. 1, the anode pad plane coupled with the field cage is housed by the top flange, and its voltages are supplied through safe high voltage connectors located on the top flange. In this study, the resistive Micromegas detector was used for electron amplification and collection. A photograph and schematic view of the pad plane are shown in Fig. 2. The Micromegas detector was fabricated at the University of Science and Technology of China using the thermal bonding technique [43]. The mesh of the Micromegas has 325 lines per inch with 23 μm diameter wires and a 49% opening rate. The avalanche gap between the mesh and the surface of the printed circuit board (PCB) is approximately 100 μm. A 5 mm thick aluminum plate was glued and screwed to the back of the PCB to increase its mechanical rigidity.

The anode pad plane has a sensitive area of $144\,\text{mm} \times 288\,\text{mm}$, consisting of 2048 readout channels. Owing to the characteristics of photodisintegration reactions, the sensitive area is segmented into 32×64 rectangular pixels, which increase in size from the inner to the outer region, as shown in Fig. 2. The pixel size in the x-direction (short

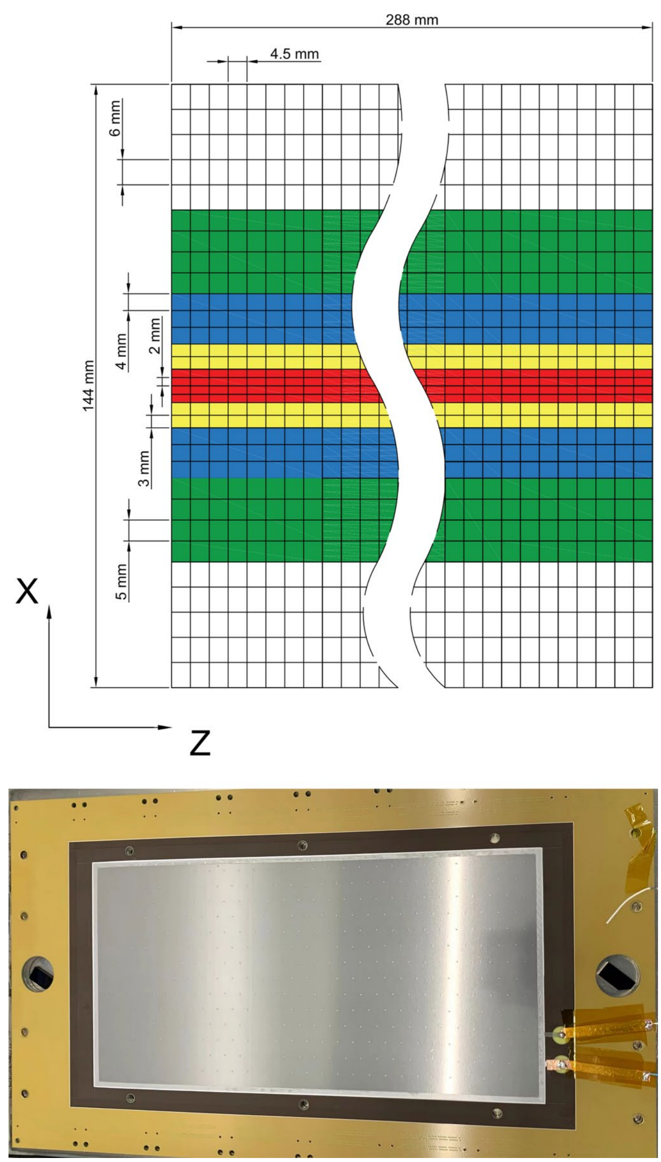

Fig. 2 Top panel: Schematic view of the sensitive area (144 mm × 288 mm) of the Micromegas plane. The sensitive area is divided into 32 × 64 rectangular pixels of different sizes. The pixel sizes in the x-direction are 2 mm, 3 mm, 4 mm, 5 mm, and 6 mm, whereas in the z-direction it is kept constant at 4.5 mm. Bottom panel: Photo of the Micromegas detector. (Color figure online)

side) increases from 2 mm to 6 mm, whereas it remains constant at 4.5 mm in the z-direction (long side). The smaller pixels in the inner region are designed to improve the angular resolution of the detector for short-range particles. The larger pixels in the outer region cause the anode pad plane to cover a larger sensitive area with a limited number of electronic channels. All pixels are read out through high-density (0.5 mm pitch) Hirose FX10A-140P/14-SV1(71) connectors containing two rows of 70 pins each. Further details on the angular resolution tests are provided in Sect. 3.3.

2.3 Field cage

The vertical uniform electric field within the sensitive volume of the TPC is formed by the field cage with a volume of 330 mm (L) × 180 mm (W) × 180 mm (H). Two versions of the field cage were developed for different experimental purposes: a double-wire-plane field cage and a PCB field cage.

The double-wire-plane field cage was designed specifically for radioactive ion beam experiments, which are known to produce high-energy reaction products. To ensure accurate measurements, designing a field cage that is transparent to both the beam ions and the reaction products while maintaining a uniform electric field is critical. Therefore, the double-wire-plane structure was selected as the most effective approach. This design features five wire planes surrounded by gold-plated tungsten wires soldered together, as shown in Fig. 3. The four-sided wire planes are composed of 70 wires, each with a diameter of 50 µm and a vertical spacing of 5.08 mm. The cathode plane is composed of 30 µm wires with a distance of 3.05 mm between each wire. The horizontal distance from the inner to the outer wire plane is 3 mm for all the wire planes. This design renders the double-wire-plane field cage nearly 99% optically transparent.

The PCB field cage was specifically designed for the photonuclear reaction experiment in SLEGS. Except for the beam entrance plane, which remained the double-wire plane, the other side planes of the PCB field cage were constructed using etched copper plate lines with a diameter of 1 mm. In this design, a 3 mm thick copper-clad PCB with dimensions of 180 mm × 330 mm serves as the cathode. The wires in the side plane are connected in series with 10 MΩ (0.1% error) surface mount resistors for both field cages to homogeneously degrade the voltage from the micromesh (GND) to the cathode (–HV). Different drift and avalanche field strengths can be set by adjusting the voltages at the cathode and anode.

To verify the uniformity of the electric field in both the field cages, a finite element calculation was performed using the neBEM code [44], which was integrated into the Garfield++ code [45]. The simulation showed that the field cage maintained the distortion of the electric field within 3% for the double-wire-plane field cage and within 1% for the PCB field cage in the sensitive volume, as shown in Fig. 4.

2.4 Readout electronics system

In view of possible future experiments, the electronic systems of the fMeta-TPC should meet requirements such as high integration, compactness, short dead time, low power consumption, and high dynamic range. The fMeta-TPC was designed for 2048 readout channels and future upgrades for higher spatial resolution, which places specific requirements on the high integration and compactness of the readout electronics. High dynamic ranges of the detected energy are also required. For example, in reactions such as $^{16}O(\gamma,\alpha)^{12}C$, the ionization energy loss ratio between ^{12}C and α can be several hundred times, requiring a wide dynamic range for charge measurement in the electronics.

The key parameters of the electronic system are listed in Table 1. It has a wide dynamic range, from 2 fC to 3 pC,

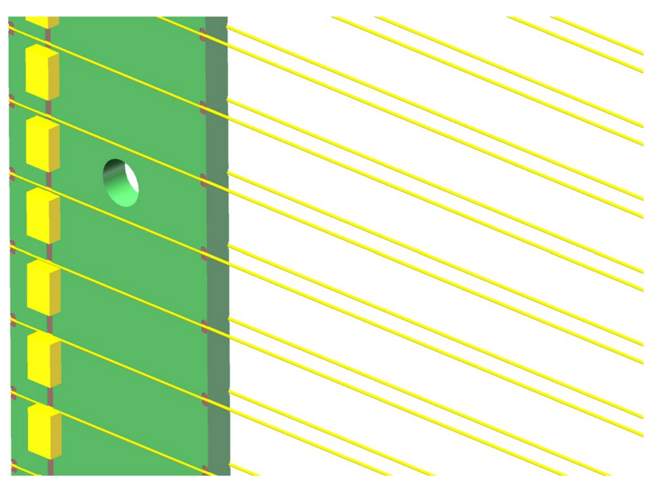

Fig. 3 3D drawing of the double layer gold-plated tungsten wire side plane of the field cage. The yellow blocks represent 10 MΩ surface mount resistors. (Color figure online)

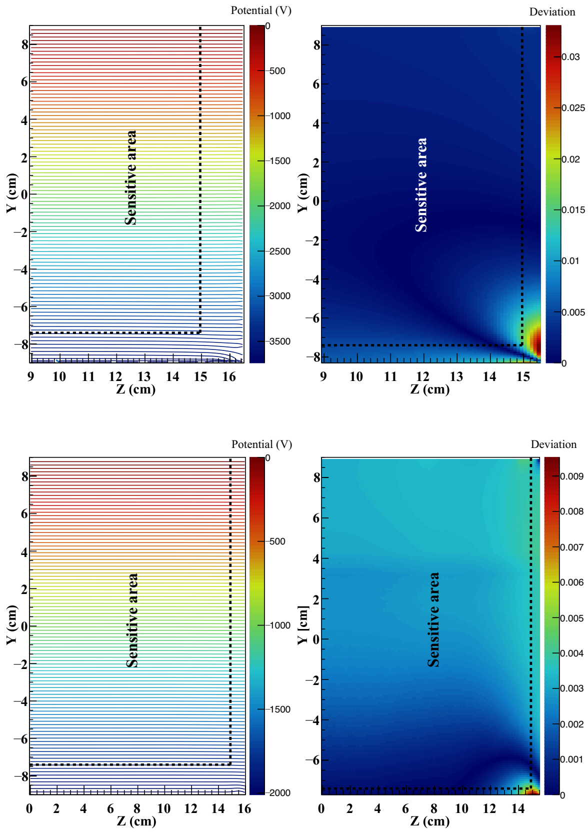

Fig. 4 Simulation of the electric potential (left) and electric field (right) of the field cage. The black dashed line marks the boundary of the sensitive area of the detector. The top two panels show the simulation results for the double-wire-plane field cage, while the bottom two panels show the simulation results for the PCB field cage. (Color figure online)

Table 1 Key parameters of the readout electronic system

Parameter	Value
Channels	2048
Dead time (μs)	25
Sampling rate (MSPS)	40
Quantization accuracy (bit)	12
Sampling window width (μs)	25.6
Dynamic range	2 fC to 3 pC

and a short dead time of 25 μs (much less than the dead time of GET electronics) for high event rates [46].

As shown in Fig. 5, the readout system is divided into two components: front- and back-end modules. The front-end module, located at the top of the chamber (as shown in Fig. 1), interfaces with the detector through two Flexible Printed Circuit (FPC) boards.

The front-end module consists of eight groups, each containing the pre-amplifier module (PAM), analog-to-digital module (ADM), and power clock management module (PCMM). Within each group, there are four PAM modules responsible for charge integration, four ADM modules responsible for waveform digitization, and one PCMM module responsible for supplying power to the front-end modules.

Upon receiving a signal from the detector, the PAM initiates amplification. A single PAM board contains 64 channels and consumes approximately 1 W of power. After amplification, the signal is transmitted to the ADM via the FPC board. The ADM then performs the simultaneous digitization of 64 channels of analog signals at a sampling rate of 40 MHz and a quantization accuracy of 12 bits. Each ADM board consumes approximately 8 W of power. Finally, the PCMM provides power and clock distribution to the group of four PAMs and ADMs.

The backend modules contains two parts: a trigger clock module (TCM) and a data concentrator module (DCM). The TCM generates a global trigger and synchronous clock by accepting hit information and distributing the trigger and synchronous clock to the DCM. The DCM is responsible for data acquisition, digital filtering, buffering, and data upload to the server via FPGA. It also distributes the synchronous clock, instructions, and triggers to the front-end electronics. In fMeta-TPC, the back-end modules have two DCMs and one TCM. Each DCM board is connected to 16 ADM boards using fiber optics.

3 Performance test

This section describes the several methods used to characterize the detector performance. The gain variation of the Micromegas detector was tested using a ^{55}Fe 5.9 keV X-ray source. A UV laser that can ionize gas molecules and form a straight line in the gas was used to study the drift velocity, field homogeneity, and intrinsic angular and positional resolutions of the detector. An ^{241}Am alpha source was used to determine the energy resolution of the detector. In this study, tests were mainly performed in Ar + CH_4 (9:1, P10 gas), Ar+iC_4H_{10} (93:7), and He + CO_2 (96:4) gas mixtures at different pressures.

3.1 Drift velocity

One of the key advantages of a TPC is its ability to record the 3D trajectories of charged particles. The determination of 3D information is based on the product of the electron drift velocity and drift time. Therefore, the accurate measurement of the electron drift velocity in a gas is crucial for particle trajectory reconstruction. In this study, the velocity

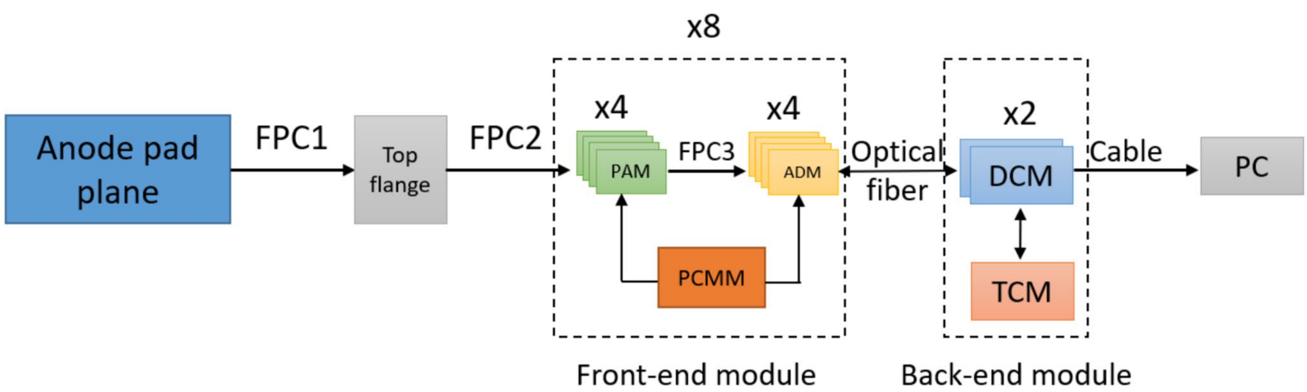

Fig. 5 Schematic of the readout electronics system. (Color figure online)

was determined using a 266 nm laser with a power of 20 mW and a frequency of 7.5 kHz. The laser entered the detector through quartz windows mounted on the front flange of the chamber, as shown in Fig. 1. Prior to the test, the orientation of the laser was determined based on the location of the incident point on the quartz window and the end point of the track in the field cage. Owing to limitations imposed by the maximum processing frequency of the ADM chip and the maximum transmission capacity of the gigabit network. Data acquisition was triggered by an external 100 Hz trigger, and the acquisition window was set to 25 µs. Considering that the pixel size remained constant at 4.5 mm in the *z*-direction, calculating the relative differences in the drift height of each pad after establishing the laser direction was possible. Therefore, one of the fired pads was chosen as the reference pad, and the drift velocity was determined by calculating the disparity in the drift height and time with respect to this reference pad.

Figure 6 shows the measured drift velocity in different gases compared with the theoretical calculations of Magboltz [44] and other experimental results [19, 47–49]. The measured results in the 600 mbar P10 gas, as shown in Fig. 6 (left), were in good agreement with other experimental results. However, a slight deviation from the theoretical results was observed when $E/P < 0.23$ V/cm/torr. The results shown in Fig. 6 (right) represent the electron drift velocities in 600 mbar Ar + iC_4H_{10} (93:7) and 500 mbar He + CO_2 (96:4) mixed gases. Both measurement results agreed with the theoretical calculations within an uncertainty of 5%. This indicated that our test method was applicable to the measurement of the electron drift velocity.

3.2 Drift field homogeneity

Ensuring homogeneity of the electric field is important for achieving accurate 3D trajectory reconstruction. Ideally, the electric field should be perpendicular to the micromesh, have no horizontal components, and maintain uniform scalar magnitude in the vertical orientation. However, practical considerations introduce several factors that

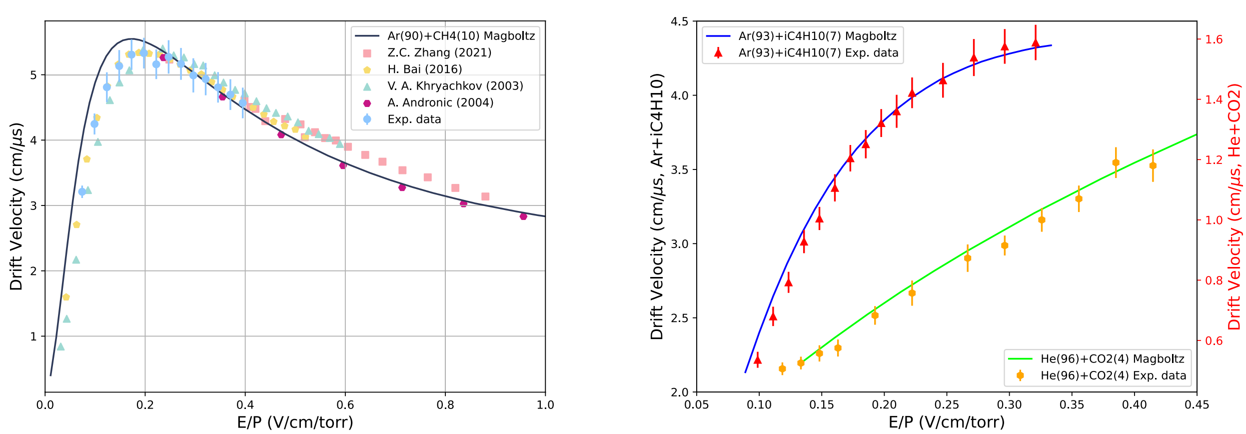

Fig. 6 Electron drift velocity measured in P10 (left), Ar+iC_4H_{10} (93:7), and He + CO_2 (96:4) gas mixtures (right). The measured data are compared with the calculations of Magboltz. Reference data are taken from studies by Z.C. Zhang [19], H. Bai [47], V.A. Khryachkov [48], A. Andronic [49]. (Color figure online)

affect the uniformity of the electric field, including wire deformation induced by voltage, feedback from positive ions, and edge effects of the electric field.

To evaluate the homogeneity of the electric field within the sensitive volume, the chamber was filled with 600 mbar of Ar + iC_4H_{10} (93:7) mixed gases. The cathode voltage was set to –1800 V, resulting in a drift electric field strength of 100 V/cm, while the anode avalanche voltage was set to 350 V. Considering that distortions are more pronounced at the edges, the uniformity of the electric field at the edge of the sensitive area better reflects the quality of the field cage design and fabrication. Therefore, two trajectories at the edges are provided as examples. In Fig. 7, the upper two panels show the measured trajectories of the laser beam along the z-axis at the edge of the sensitive area, with the red lines representing two-dimensional weighted linear fits.

The two lower panels of Fig. 7 present the distributions of the residual distances between the two-dimensional linear fitting curves and the measured positions on the anode pad plane. The residual distance d_i can be computed as follows:

$$d_i = \frac{|ax_i + by_i + c|}{\sqrt{a^2 + b^2}},$$

where a and b are the fitting parameters of the two-dimensional weighted linear fits, and x_i and y_i are the fired pixel positions on the anode pad plane. As shown in the lower panels of Fig. 7, the standard deviation of the residual distance distributions remained below 0.4 mm for both measurements, indicating that the electric field in the sensitive area was almost perpendicular to the micromesh and lacked a significant horizontal component.

3.3 Angular and spatial resolution

Because UV laser light is free of straggling effects, it can be used to test the intrinsic angular and spatial resolutions of the detector. In this study, θ is defined as the angle between the projection of the track on the readout plane and the z axis. The detector was filled with Ar + iC_4H_{10} (93:7) gas mixture at 400 mbar. During the measurement, the drift field strength was set to 44 V/cm and the avalanche voltage was

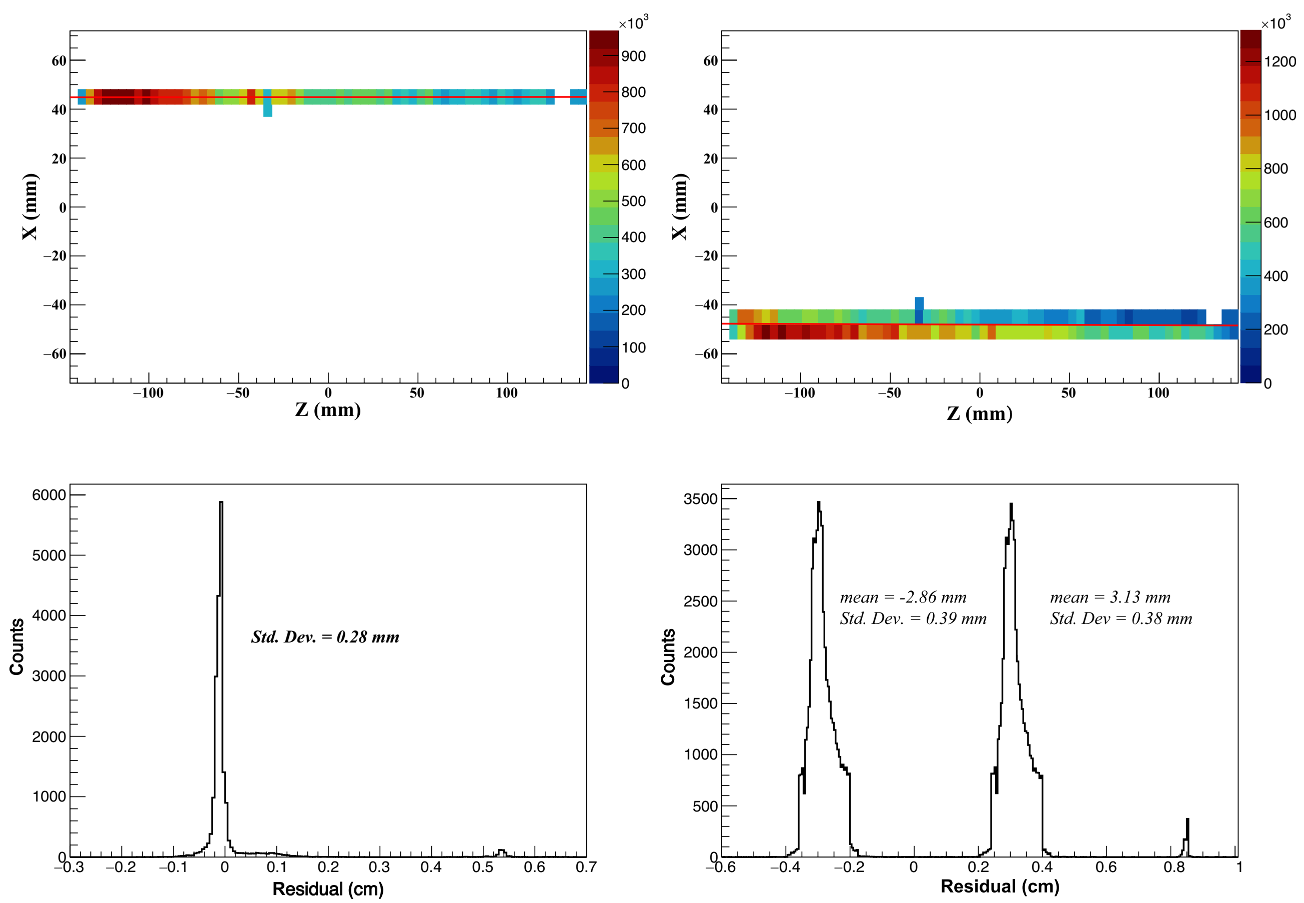

Fig. 7 The top two panels show the recorded two-dimensional trajectories of the laser beam, with the red lines representing two-dimensional weighted linear fits. The lower panel shows the residuals between the fitted curve and the measured positions. (Color figure online)

set to 345 V. Figure 8 (top) shows the measured angular resolution of the laser with an incident angle of 6.05°. An angular resolution of 0.17° (σ_θ) was achieved in this incident direction. The incident angle of the laser beam was determined by three-dimensional weighted linear fitting, with the weighted coefficient being the ratio of the deposited charge to the pixel area.

Notably, both angular and spatial resolutions depend on the angle of incidence and the pad structure. Therefore, measuring the intrinsic angular resolutions at different incident angles was necessary, particularly for readout pixels of different sizes, as shown in Fig. 2. Figure 8 shows the measured intrinsic angular resolution with the laser light incident through two quartz windows at different angles of incidence. A remarkable angular resolution of 0.06° (σ_θ) was achieved at an angle of incidence of 5.6°, whereas the worst measured angular resolution remained within 0.30° (σ_θ) when the laser mainly traversed the pixel with a size of 6 mm × 4.5 mm.

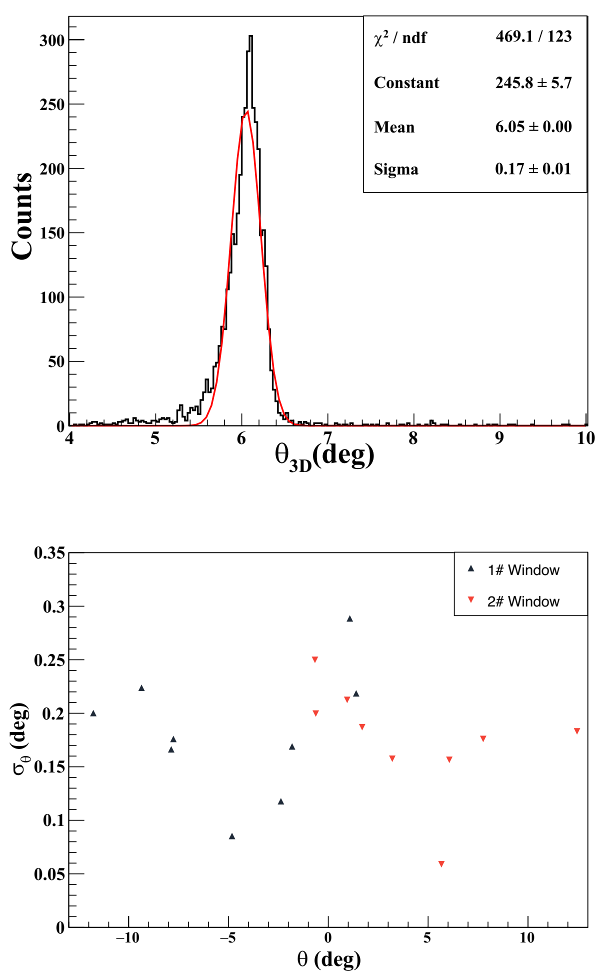

Fig. 8 Top panel: Angular distribution of the laser track determined by weighted linear fitting. Bottom panel: Intrinsic angular resolutions measured for laser incidences at different angles from two symmetrically positioned quartz windows. (Color figure online)

For the detector with a sensitive length of 288 mm, the corresponding position resolutions (FWHM) can be derived from 288 × 2.355σ_θ. Thus, the optimal position resolution was 0.7 mm and the worst resolution was within 3.4 mm.

3.4 Gain uniformity

Calibration of the gain map plays a critical role in energy reconstruction of charged particles. In addition, the uniformity of the detector is primarily influenced by two factors. The primary factor is the uniformity of the avalanche gap, while the secondary factor is the uniformity of the electronic gain.

First, the gain variations in the electronics were tested by applying a common pulse to the PAM board. In each PAM module, all 64 channels were connected to the Sub-Miniature-A connector via 1 pF capacitors with 5% accuracy for gain calibration. The resulting waveform acquired from the 64 channels within the PAM module is visually represented in the top panel of Fig. 9. By adjusting the pulse amplitudes to record the waveform amplitudes for each channel at different collected charge levels, the resulting normalized gain variation distribution for each channel is shown in the bottom panel of Fig. 9. The results showed that the gain variation across the 2048 channels of the electronic system was within 4% (σ/μ).

An ^{55}Fe X-ray source with an activity of 1.43×10^5 becquerels and a diameter of 10 mm was used to evaluate the gain uniformity of the Micromegas detector. The source was positioned at the center of the bottom flange, at a distance of 20 cm from the micromesh. This ensured that every pixel was illuminated. For the gain uniformity test, the chamber was filled with P10 gas at a pressure of 600 mbar. The anode voltage was set to 465 V, and the field ratio of the avalanche field to the drift field was set to 300, ensuring that more than 95% of the primary electrons could be collected in the avalanche gap at this field ratio.

$$\begin{bmatrix} x_1 & x_2 & \cdots & x_{2048} \\ x_1^2 & x_2^2 & \cdots & x_{2048}^2 \\ \cdots & \cdots & \vdots & \cdots \\ x_1^m & x_2^m & \cdots & x_{2048}^m \end{bmatrix} \begin{bmatrix} \theta_1 \\ \theta_2 \\ \vdots \\ \theta_{2048} \end{bmatrix} = \begin{bmatrix} y_1 \\ y_2 \\ \vdots \\ y_m \end{bmatrix} \tag{1}$$

Owing to the transverse diffusion of electrons, a typical 5.9 keV X-ray event consists of 2–7 pixels. To calculate the gain value for each pixel, multiple linear regression was used to analyze the data. In Eq. (1), the input matrix on the left represents the deposited charge of each pixel for each ^{55}Fe event. The middle parameter, vector $\boldsymbol{\theta}$, represents the gain map of the detector, and the output vector $\boldsymbol{Y}$ represents the primary electrons ionized by the 5.9 keV X-rays. According to the method of least squares, the parameter vector can be calculated from $\boldsymbol{\theta} = (\boldsymbol{X}^{\mathrm{T}}\boldsymbol{X})^{-1} \cdot \boldsymbol{X}^{\mathrm{T}}\boldsymbol{Y}$. The resulting gain map, as shown in Fig. 10 (left), revealed a gain variation

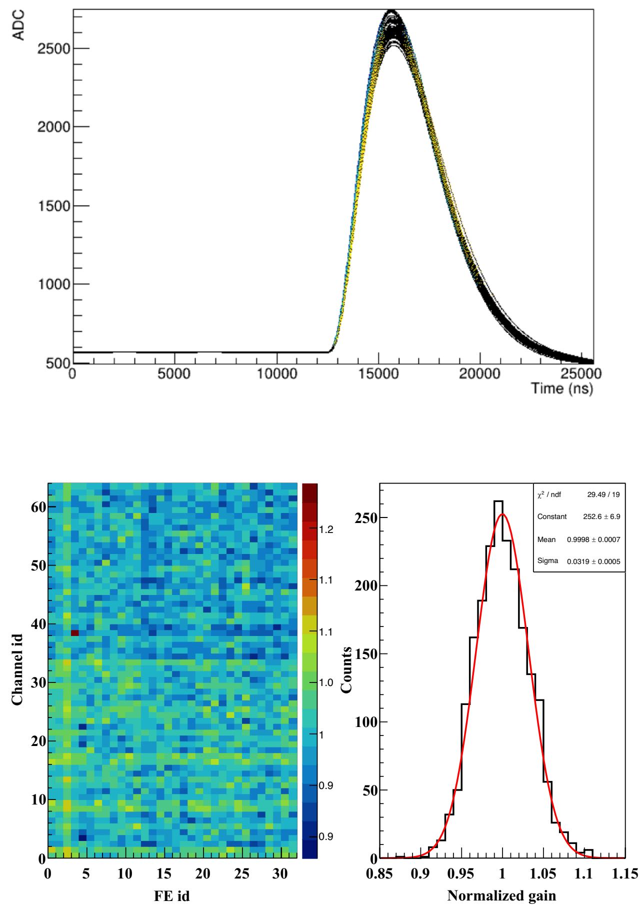

Fig. 9 Top panel: 64-channel waveforms acquired from a PAM by injecting a common pulse. Bottom panel: (Left) Channel-by-channel gain variations of the electronics. (Right) Normalized gain distribution of the 2048 channels. (Color figure online)

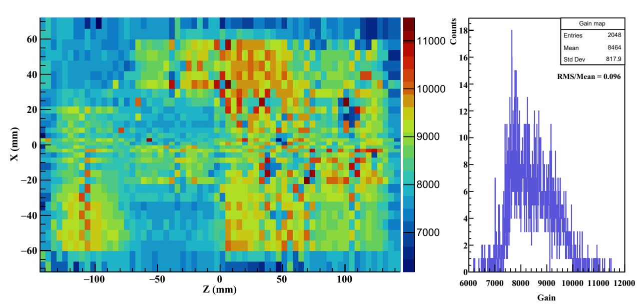

Fig. 10 (Left) Gain map of the detector at the avalanche voltage of 465 V. The color scale represents the gain of each pad. (Right) Gain distribution of the 2048 pads. (Color figure online)

of approximately 9.6% (RMS/mean) over 2048 channels. This result implied that the fluctuations in detector gain were primarily caused by the nonuniformity of the detector's avalanche gaps.

To validate the results obtained, the gain map was adjusted to correct the ^{55}Fe spectrum measured at the anode. A comparison of the spectrum before and after the correction is shown in Fig. 11. The spectrum before correction was derived assuming a uniform pixel gain. After applying the gain map, the width (σ) of the ^{55}Fe spectrum decreased from 1.03 to 0.92 keV, indicating that the gain map obtained by multiple linear regression had some reliability.

3.5 Energy resolution

The energy resolution of the detector was further investigated using an ^{241}Am alpha source located 39 mm from the sensitive region. The detector was filled with 600 mber P10 gas, and the voltages applied to the anode and cathode were set to 405 V and –2430 V, respectively. The total charge deposited by the alpha particles was obtained on an event-by-event basis by summing all the individual charges collected on each pad. To minimize the effect of the dead zone between the alpha source and the sensitive area on the energy resolution, the alpha source had to be collimated by restricting the emission angle of alpha to within ±5° during data analysis. The resulting energy spectrum for the alpha source is shown in Fig. 12. Fitting the spectrum to a single Gaussian distribution yielded an energy resolution of 6.85% for the alpha particles with a deposited energy of 3.0 MeV.

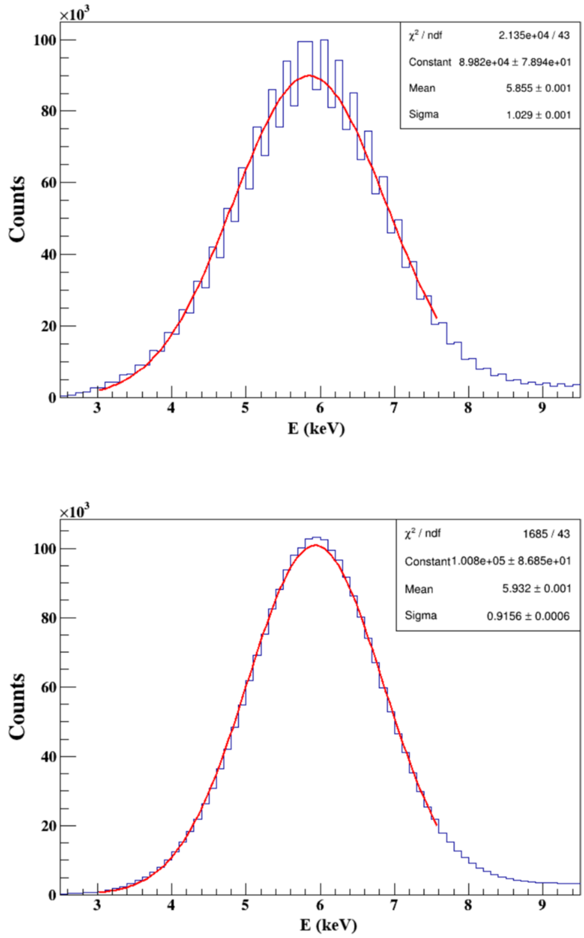

Fig. 11 Top Panel: ^{55}Fe spectrum without gain map. Bottom Panel: ^{55}Fe spectrum with the correction of gain map. (Color figure online)

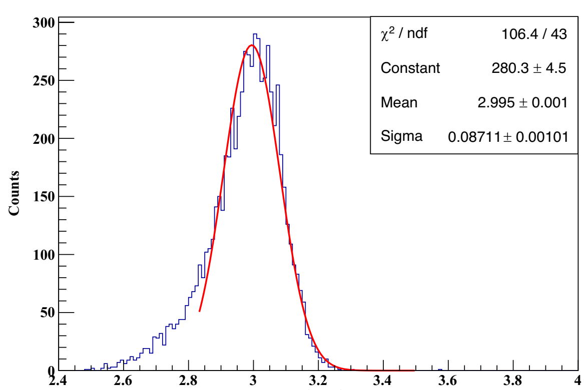

Fig. 12 Energy spectrum obtained from ^{241}Am source. (Color figure online)

4 Summary

A new 2048-channel prototype active target detector system, fMeta-TPC, was designed and constructed for low-energy nuclear experiments. In this study, a resistive Micromegas with an avalanche gap of 100 μm was used for signal readout. As verified by an ^{55}Fe X-ray source, the gain uniformity of the detector was approximately 10% (RMS/mean), and the contribution of the electronic gain fluctuations was within 4% (σ/μ). The energy resolution obtained from the total charge collected on the pad plane was deduced to be 6.85% for 3.0 MeV alpha particles.

Considering the characteristics of photodisintegration reactions, the readout plane was divided into 2048 rectangular pixels of unequal sizes. It was tested with laser light at different injection angles to evaluate the effect of pad size on angular resolution. The results showed that the readout board can achieve a remarkable angular resolution of 0.06° (σ_θ); the worst angular resolution measured was within 0.30° (σ_θ). In addition, the electron drift velocity and homogeneity of the drift field by the laser light were also tested. The results showed that the homogeneity of the drift field was satisfactorily maintained in the sensitive volume. The measured electron drift velocity was in good agreement with other experimental results and theoretical calculations.

For future low-pressure experiments, the plan is to upgrade the detection system by using a Micromegas detector with a double micromesh gaseous structure [50, 51] or with a larger avalanche gap. In addition, the first commissioning run of the ^{7}Li (γ, t) ^{4}He ground-state cross section was performed at SLEGS, and the data are currently being processed.

Author contributions All authors contributed to the study conception and design. Material preparation, data collection and analysis were performed by Huang-Kai Wu, Xi-Yang Wang, Yu-Miao Wang and You-Jing Wang. The first draft of the manuscript was written by Huang-Kai Wu, and all authors commented on previous versions of the manuscript. All authors read and approved the final manuscript.

Data availability The data that support the findings of this study are openly available in Science Data Bank at https://cstr.cn/31253.11.sciencedb.j00186.00274 and https://doi.org/10.57760/sciencedb.j00186.00274.

Declarations

Conflict of interest Yu-Gang Ma, De-Qing Fang and Xi-Guang Cao are the editorial board members for Nuclear Science and Techniques and are not involved in the editorial review, or the decision to publish this article. All authors declare that there are no conflict of interest.

References

1. H.W. Wang, G.T. Fan, L.X. Liu et al., Commissioning of laser electron gamma beamline SLEGS at SSRF. Nucl. Sci. Tech. **33**, 87 (2022). https://doi.org/10.1007/s41365-022-01076-0
2. NewSUBARU BL01, Laser compton gamma source. https://www.lasti.u-hyogo.ac.jp/NS-en/facility/bl01/
3. High intensity gamma-ray source (HIGS). https://tunl.duke.edu/research/our-facilities
4. A.M. Sandorfi, M.J. LeVine, C.E. Thorn et al., High energy gamma ray beams from Compton backscattered laser light. IEEE Trans. Nucl. Sci. **30**, 3083–3087 (1983). https://doi.org/10.1109/TNS.1983.4336577
5. Extreme light infrastructure–nuclear physics (ELI-NP). www.eli-np.ro
6. B.S. Huang, Y.G. Ma, W.B. He, Photonuclear reaction as a probe for α-clustering nuclei in the quasi-deuteron region. Phys. Rev. C **95**, 034606 (2017). https://doi.org/10.1103/PhysRevC.95.034606
7. B.S. Huang, Y.G. Ma, W.B. He, Alpha-clustering effects on $^{16}O(\gamma, np)^{14}N$ in quasi-deuteron region. Eur. Phys. J. A **53**, 119 (2017). https://doi.org/10.1140/epja/i2017-12300-0
8. B.S. Huang, Y.G. Ma, Two-proton momentum correlation from photodisintegration of α-clustering light nuclei in the quasi-deuteron region. Phys. Rev. C **101**, 034615 (2020). https://doi.org/10.1103/PhysRevC.101.034615
9. Y. Ayyad, N. Abgrall, T. Ahn et al., Next-generation experiments with the active target time projection chamber (AT-TPC). Nucl. Instrum. Meth. A **954**, 161341 (2020). https://doi.org/10.1016/j.nima.2018.10.019
10. D. Bazin, T. Ahn, Y. Ayyad et al., Low energy nuclear physics with active targets and time projection chambers. Prog. Part. Nucl. Phys. **114**, 103790 (2020). https://doi.org/10.1016/j.ppnp.2020.103790
11. S. Beceiro-Novo, T. Ahn, D. Bazin et al., Active targets for the study of nuclei far from stability. Prog. Part. Nucl. Phys. **84**, 124–165 (2015). https://doi.org/10.1016/j.ppnp.2015.06.003
12. J. Bradt, D. Bazin, F. Abu-Nimeh et al., Commissioning of the active-target time projection chamber. Nucl. Instrum. Meth. A **875**, 65–79 (2017). https://doi.org/10.1016/j.nima.2017.09.013
13. W.R. Zimmerman, M.W. Ahmed, B. Bromberger et al., Unambiguous identification of the second 2^+ State in ^{12}C and The structure of the Hoyle state. Phys. Rev. Lett. **110**, 152502 (2013). https://doi.org/10.1103/PhysRevLett.110.152502
14. R. Smith, M. Gai, S.R. Stern et al., Precision measurements on oxygen formation in stellar helium burning with gamma-ray beams and a time projection chamber. Nat. Commun. **12**, 5920 (2021). https://doi.org/10.1038/s41467-021-26179-x
15. K. Miernik, W. Dominik, Z. Janas et al., Two-proton correlations in the decay of ^{45}Fe. Phys. Rev. Lett. **99**, 192501 (2007). https://doi.org/10.1103/PhysRevLett.99.192501
16. T. Furuno, T. Kawabata, S. Adachi et al., Neutron quadrupole transition strength in ^{10}C deduced from the $^{10}C(\alpha, \alpha')$ measurement with the MAIKo active target. Phys. Rev. C **100**, 054322 (2019). https://doi.org/10.1103/PhysRevC.100.054322
17. M. Murata, T. Kawabata, S. Adachi et al., Photodisintegration cross section of ^{4}He in the giant dipole resonance energy region. Phys. Rev. C **107**, 064317 (2023). https://doi.org/10.1103/PhysRevC.107.064317
18. L.S. Yang, J.Y. Xu, Q.T. Li et al., Performance of the CAT-TPC based on two-dimensional readout strips. Nucl. Sci. Tech. **32**, 85 (2021). https://doi.org/10.1007/s41365-021-00919-6
19. Z.C. Zhang, X.Y. Wang, T.L. Pu et al., Studying the heavy-ion fusion reactions at stellar energies using time projection chamber. Nucl. Instrum. Meth. A **1016**, 165740 (2021). https://doi.org/10.1016/j.nima.2021.165740
20. X.Y. Wang, N.T. Zang, Z.C. Zhang et al., Studies of the 2α and 3α channels of the $^{12}C + ^{12}$ reaction in the range of E_{cm} = 8.9 MeV to 21 MeV using the active target time projection chamber. Chinese Phys. C **46**, 104001 (2022). https://doi.org/10.1088/1674-1137/ac7a1d
21. W. Jia, Y. Lv, Z. Zhang et al., Gap uniformity study of a resistive micromegas for the multi-purpose time projection chamber (MTPC) at back-n white neutron source. Nucl. Instrum. Meth. A **1039**, 167157 (2022). https://doi.org/10.1016/j.nima.2022.167157
22. Y. Li, H. Yi, Y. Sun et al., Performance study of the multi-purpose time projection chamber (MTPC) using a four-component alpha source. Nucl. Instrum. Meth. A **1060**, 169045 (2024). https://doi.org/10.1016/j.nima.2023.169045
23. J. Bishop, C.E. Parker, G.V. Rogachev et al., Neutron-upscattering enhancement of the triple-alpha process. Nat. Commun. **13**, 2151 (2022). https://doi.org/10.1038/s41467-022-29848-7
24. M. Freer, H.O.U. Fynbo, The Hoyle state in ^{12}C. Prog. Part. Nucl. Phys. **78**, 1–23 (2014). https://doi.org/10.1016/j.ppnp.2014.06.001
25. W.B. He, Y.G. Ma, X.G. Cao et al., Giant dipole resonance as a fingerprint of α clustering configurations in ^{12}C and ^{16}O. Phys. Rev. Lett. **113**, 032506 (2014). https://doi.org/10.1103/PhysRevLett.113.032506
26. R. Bijker, F. Iachello et al., Cluster structure of light nuclei. Prog. Theor. Exp. Phys. **110**, 103735 (2020). https://doi.org/10.1016/j.ppnp.2019.103735
27. Y.G. Ma, Effects of α-clustering structure on nuclear reaction and relativistic heavy-ion collisions. Nucl. Tech. (in Chinese) **46**, 080001 (2023). https://doi.org/10.11889/j.0253-3219.2023.hjs.46.080001
28. Y.G. Ma, S. Zhang, α-clustering effects in relativistic heavy-ion collisions. Sci. Sin. Phys. Mech. Astron. (in Chinese) **54**, 292004 (2024). https://doi.org/10.1360/SSPMA-2024-0013
29. L. Yang, C.J. Lin, H.M. Jia et al., Progress on nuclear reactions and related nuclear structure at low energies. Nucl. Tech. (in Chinese) **46**, 080006 (2023). https://doi.org/10.11889/j.0253-3219.2023.hjs.46.080006
30. D.Q. Fang, Neutron skin thickness and its effects in nuclear reactions. Nucl. Tech. (in Chinese) **46**, 080016 (2023). https://doi.org/10.11889/j.0253-3219.2023.hjs.46.080016
31. Y. Chen, Y.L. Ye, K. Wei, Progress and perspective of the research on exotic structures of unstable nuclei. Nucl. Tech. (in Chinese) **46**, 080020 (2023). https://doi.org/10.11889/j.0253-3219.2023.hjs.46.080020
32. F. Hoyle, D.N.F. Dunbar, W.A. Wenzel et al., A state in C-12 predicted from astrophysical evidence. Phys. Rev. **92**, 1095–1095 (1953)
33. R. Smith, T. Kokalova, C. Wheldon et al., New measurement of the direct 3α decay from the ^{12}C Hoyle state. Phys. Rev. Lett. **119**, 132502 (2017). https://doi.org/10.1103/PhysRevLett.119.132502
34. R. Smith, M. Gai, M.W. Ahmed et al., Stringent upper limit on the direct 3α decay of the Hoyle state in ^{12}C. Phys. Rev. C **101**, 021302 (2020). https://doi.org/10.1103/PhysRevC.101.021302
35. A. Tohsaki, H. Horiuchi, P. Schuck et al., Alpha cluster condensation in ^{12}C and ^{16}O. Phys. Rev. Lett. **87**, 3177 (1998). https://doi.org/10.1103/PhysRevLett.87.192501
36. G. Röpke, A. Schnell, P. Schuck et al., Four-particle condensate in strongly coupled fermion systems. Phys. Rev. Lett. **80**, 192501 (2001). https://doi.org/10.1103/PhysRevLett.80.3177
37. J.H. Chen, Y.L. Ye, K. Ma et al., New evidence of the Hoyle-like structure in ^{16}O. Sci. Bull. **68**, 1119–1126 (2023). https://doi.org/10.1016/j.scib.2023.04.031
38. P.W. Zhao, N. Itagaki, J. Meng, Rod-shaped nuclei at extreme spin and isospin. Phys. Rev. Lett. **115**, 022501 (2015). https://doi.org/10.1103/PhysRevLett.115.022501

39. E. Epelbaum, H. Krebs, T.A. Lahde et al., Structure and rotations of the Hoyle state. Phys. Rev. Lett. **109**, 252501 (2012). https://doi.org/10.1103/PhysRevLett.109.252501
40. E. Uegaki, S. Okabe, Y. Abe et al., Structure of the excited states in ^{12}C. Prog. Theor. Exp. Phys. **57**, 1262–1276 (1977). https://doi.org/10.1143/PTP.57.1262
41. B. Zhou, Y. Funaki, H. Horiuchi et al., The 5α condensate state in ^{16}Ne. Nat. Commun. **14**, 8206 (2023). https://doi.org/10.1038/s41467-023-43816-9
42. B.S. Huang, Y.G. Ma, Dipole excitation of ^{6}Li and ^{9}Be studied with an extended quantum molecular dynamics model. Phys. Rev. C **103**, 054318 (2021). https://doi.org/10.1103/PhysRevC.103.054318
43. J. Feng, Z. Zhang, J. Liu et al., A thermal bonding method for manufacturing Micromegas detectors. Nucl. Instrum. Meth. A **989**, 164958 (2021). https://doi.org/10.1016/j.nima.2020.164958
44. R. Veenhof, K. Baraka, S. Caiazza et al., Garfield++. https://garfieldpp.web.cern.ch/garfieldpp/
45. S. Mukhopadhay, N. Majumdar, A nearly exact boundary element method. https://nebem.web.cern.ch/nebem/
46. Z. Chen, C. Feng, H. Chen et al., Readout system for a prototype multi-purpose time projection chamber at CSNS Back-n. J. Instrum. **17**, P05032 (2022). https://doi.org/10.1088/1748-0221/17/05/P05032
47. H. Bai, Z. Wang, L. Zhang et al., A method for measuring the electron drift velocity in working gas using a Frisch-grid ionization chamber. Nucl. Instrum. Meth. A **840**, 36–41 (2016). https://doi.org/10.1016/j.nima.2016.09.049
48. V.A. Khryachkov, I.V. Dunaeva, M.V. Dunaev et al., A method for rapid measurements of working-gas properties in a pulse ionization chamber. Instrum. Exp. Tech. **46**, 804–813 (2003). https://doi.org/10.1023/B:INET.0000008936.97013.4d
49. A. Andronic, S. Biagi, P. Braun-Munzinger et al., Drift velocity and gain in argon- and xenon-based mixtures. Nucl. Instrum. Meth. A **523**, 302–308 (2004). https://doi.org/10.1016/j.nima.2003.11.426
50. Z. Zhang, B. Qi, C. Liu et al., A high-gain, low ion-backflow double micro-mesh gaseous structure for single electron detection. Nucl. Instrum. Meth. A **889**, 78–82 (2018). https://doi.org/10.1016/j.nima.2018.02.006
51. B. Qi, K. Liang, Z. Zhang et al., Optimization of the double micro-mesh gaseous structure (DMM) for low ion-backflow applications. Nucl. Instrum. Meth. A **976**, 164282 (2020). https://doi.org/10.1016/j.nima.2020.164282